International Journal of Engineering Research and Development
e- ISSN: 2278-067X, p-ISSN: 2278-800X, www.ijerd.com
Volume 22, Issue 9 (September 2026), PP 124-134

Computational Fluid Dynamics Analysis of Temperature Uniformity in a Large Climatic Chamber under Multiple Temperature Conditions

Yu Shao
Huaibei Mining Co., Ltd., Qinan Coal Mine
Huaibei, Anhui, China
Corresponding Author: Yu Shao

ABSTRACT: *Temperature uniformity is an important indicator of the environmental regulation performance of large climatic chambers. In this study, a transient computational fluid dynamics model of a climatic chamber equipped with a closed-loop circulating air-supply system was developed using Fluent. The standard k-ε turbulence model was adopted, and ten axial-flow fans with a diameter of 0.85 m were represented by velocity-inlet boundary conditions. The total circulating airflow rate was 300,000 m^3/h Five target temperatures of -40, -10, 0, 45, and 60°C were investigated. Temperature data from 13 monitoring points and three repeated numerical calculations were used to evaluate the temperature range, maximum deviation from the target temperature, and temperature fluctuation. The results showed that the circulating airflow formed a continuous closed-loop flow path through the test zone and the surrounding return-air gallery under all operating conditions. The temperature range and maximum temperature deviation were 0.016–0.106°C, while the temperature fluctuation was 0.007–0.053°C. The most uniform temperature field was obtained at 0°C, whereas the largest spatial variation occurred at 45°C. Local temperature differences were mainly observed near the central transition section and airflow turning regions. These results demonstrate that the proposed circulating air-supply system can maintain a relatively uniform temperature field over a wide operating temperature range and provide a numerical basis for optimizing airflow organization in large climatic chambers.*
KEY WORDS: *large climatic chamber; computational fluid dynamics; temperature uniformity; airflow organization*

Date of Submission: 09-09-2026 Date of acceptance: 18-09-2026

I. INTRODUCTION

Climatic chambers are widely used to reproduce controlled temperature and airflow conditions for environmental testing of vehicles, materials, components, and engineering systems. Compared with outdoor testing, chamber-based testing reduces the influence of unpredictable weather and allows products to be evaluated under repeatable low- and high-temperature conditions. However, increasing chamber size also increases the airflow circulation distance and internal volume, making it more difficult to maintain a uniform thermal environment throughout the usable test zone [1–3].

The thermal environment inside a climatic chamber is affected by the arrangement of heating and cooling equipment, fan airflow, supply and return paths, and internal geometry. Reaching the target temperature does not necessarily indicate that the entire test zone has reached a uniform state. Local recirculation, insufficient air mixing, and flow separation near structural components may produce spatial temperature differences. Previous experimental and numerical studies have shown that inlet position, airflow organization, and chamber configuration can substantially influence the distributions of temperature and humidity [4–6]. Therefore, analysing only the temperature at a limited number of monitoring points may not fully reveal the thermal characteristics of a large chamber.

Computational fluid dynamics (CFD) provides an effective approach for investigating airflow and heat transfer in enclosed environmental facilities. It can predict three-dimensional velocity and temperature fields and identify local regions that are difficult to characterize using point measurements alone. CFD has been applied to analyse fan-induced airflow, temperature distribution, draught risk, and circulation performance in vehicle climatic chambers and other controlled environments [7–10]. Related studies of mixing ventilation, indoor environmental systems, and plant factories have further demonstrated that fan arrangement, inlet conditions, and flow-path design strongly affect air mixing and spatial uniformity [11–15]. These investigations provide useful methods for chamber analysis, but the temperature uniformity of a large closed-loop climatic chamber over a wide operating range from deep cooling to high-temperature conditions still requires system-specific evaluation.

In this study, a three-dimensional transient CFD model of a large climatic chamber was established using ANSYS Fluent. The chamber contained a surrounding return-air gallery and ten axial-flow fans that formed the main circulation system. Five target temperatures of −40, −10, 0, 45, and 60 °C were considered. The airflow pathlines and static-temperature fields were analysed, and the temperature characteristics of 13 monitoring points were evaluated using the spatial temperature range R_t, maximum temperature deviation D_t, and repeatability half-range F_t. The objective was to characterize the airflow organization and temperature uniformity of the chamber under different operating conditions and to provide a numerical basis for optimizing its circulation-system configuration.

II. MATERIAL AND METHODS

2.1 Chamber configuration and operating conditions

The computational domain was established according to the three-dimensional structure of the large climatic chamber. The usable test zone measured 9.6 m × 6.9 m × 10.0 m. A surrounding air gallery with a height of 8 m was arranged outside the test zone to form the main return-air passage. The principal geometric features affecting airflow circulation were retained, whereas small structural details with limited influence on the main flow were omitted.

Ten axial-flow fans, each with a diameter of 0.85 m, were installed in the air-conditioning section. The total circulation airflow rate was 300,000 m³/h and was evenly distributed among the fans. Therefore, the airflow rate of each fan was 30,000 m³/h, corresponding to an inlet velocity of approximately 14.69 m/s. The airflow passed through the test zone and returned through the surrounding gallery, forming a closed circulation path. The chamber structure, fan arrangement, and nominal airflow direction are shown in Figure 1.

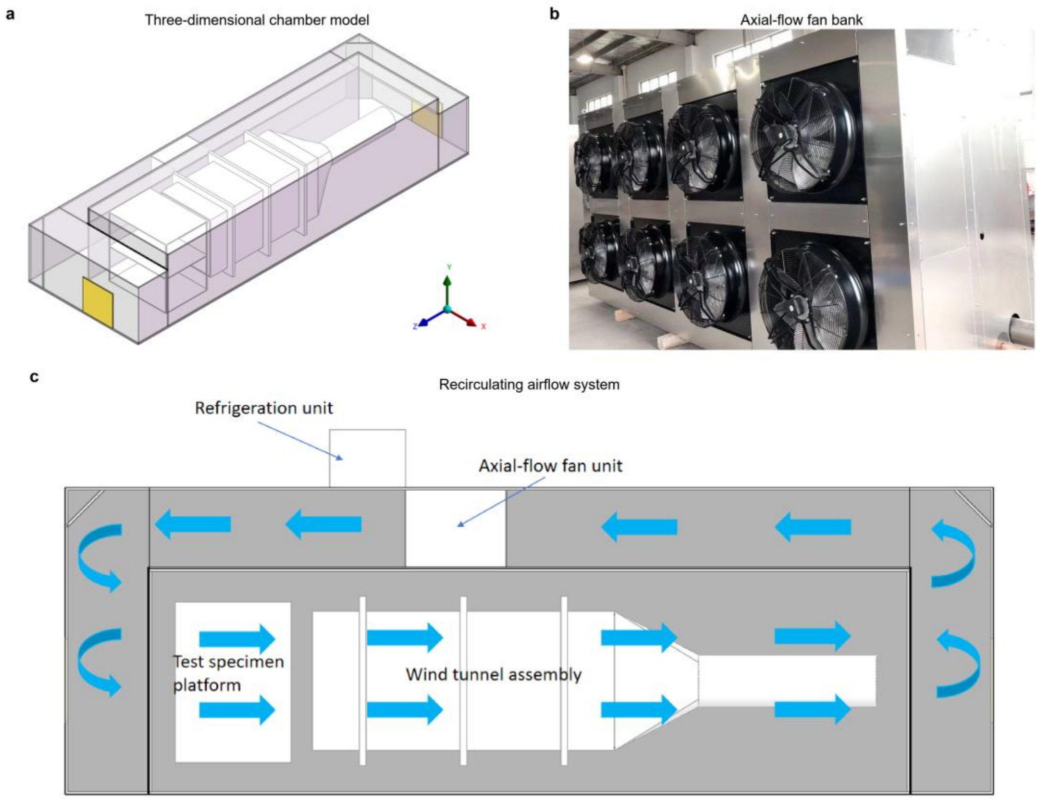

Figure 1: Structure of the climatic chamber and recirculating airflow system: (a) simplified three-dimensional model; (b) axial-flow fan unit; (c) schematic of the recirculating airflow system.

The initial air temperature inside the chamber was set to 30 °C. Five target-temperature conditions, namely −40, −10, 0, 45, and 60 °C, were investigated. The target temperature of each condition was imposed through the fan inlet temperature. Except for the inlet temperature, the chamber geometry, fan velocity, and other numerical settings remained unchanged among the five cases.

Table 1. Main geometric and operating parameters of the climatic chamber

Parameter	Value
Test-zone dimensions	9.6 m × 6.9 m × 10.0 m
Height of surrounding air gallery	8 m
Number of axial-flow fans	10
Fan diameter	0.85 m
Total circulation airflow rate	300,000 m³/h
Airflow rate of each fan	30,000 m³/h
Fan inlet velocity	14.69 m/s
Initial chamber temperature	30 °C
Target temperatures	−40, −10, 0, 45, and 60 °C

2.2 Numerical model and calculation settings

The airflow and heat-transfer processes inside the chamber were simulated using ANSYS Fluent 2022 R2. A transient pressure-based solver was employed, and the energy equation was enabled to calculate the temperature field. The standard *k*–*ε* turbulence model was used to describe the turbulent airflow because of its numerical stability and applicability to engineering ventilation flows [16]. Pressure–velocity coupling was performed using the SIMPLE algorithm.

The governing equations included the continuity, momentum, and energy equations:

$$\frac{\partial \rho}{\partial t} + \nabla \cdot (\rho \mathrm{u}) = 0$$

$$\frac{\partial (\rho \mathrm{u})}{\partial t} + \nabla \cdot (\rho \mathrm{uu}) = -\nabla p + \nabla \cdot \boldsymbol{\tau}$$

$$\frac{\partial (\rho E)}{\partial t} + \nabla \cdot [\mathrm{u}(\rho E + p)] = \nabla \cdot (k_{\mathrm{eff}} \nabla T)$$

where ρ is the air density, t is time, u is the velocity vector, p is the static pressure, $\boldsymbol{\tau}$ is the stress tensor, E is the total energy, k_{eff} is the effective thermal conductivity, and T is the air temperature.

The ten axial-flow fans were represented by velocity-inlet boundaries. The inlet velocity was set to 14.69 m/s, and the inlet temperature was assigned according to the target temperature of each numerical case. The chamber walls were treated as adiabatic boundaries. Gravity, buoyancy, and radiation were not considered.

The computational domain was discretized using tetrahedral cells. The final mesh contained 2,154,753 cells, with a reported mesh quality of 0.879. The same mesh and numerical configuration were used for all five target-temperature conditions to maintain consistent spatial resolution.

Table 2. Main settings of the numerical model.

Numerical setting	Specification
Calculation type	Transient
Solver	Pressure-based solver
Turbulence model	Standard *k*–*ε*
Pressure–velocity coupling	SIMPLE
Energy equation	Enabled
Fan boundary condition	Velocity inlet
Fan inlet velocity	14.69 m/s
Inlet temperature	Corresponding target temperature
Chamber-wall boundary	Adiabatic
Gravity and buoyancy	Not considered
Radiation	Not considered
Mesh type	Tetrahedral
Number of cells	2,154,753
Reported mesh quality	0.879

2.2 Monitoring points and evaluation metrics

Thirteen temperature-monitoring points were arranged in the usable test zone to evaluate the spatial temperature distribution. Nine monitoring points were distributed at three representative heights, and four additional points were arranged at the centres of the side boundaries. The monitoring-point arrangement is shown in Figure 2.

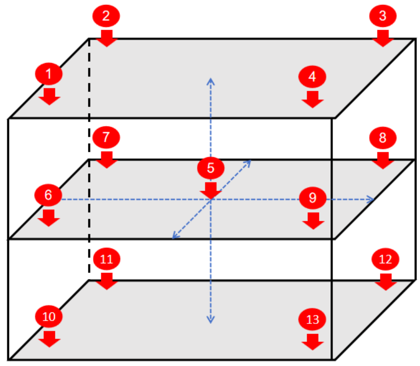

Figure 2: Arrangement of the original monitoring points in the test zone.

Three repeated numerical calculations were performed for each monitoring point under each target-temperature condition. Let T_{ij} represent the calculated temperature at monitoring point i in the j-th repeated calculation, where i=1,2,...,13 and j=1,2,3. The mean temperature at each monitoring point was calculated as

$$\bar{T}_i = \frac{1}{3}\sum_{j=1}^{3} T_{ij}.$$

The spatial temperature range R_t, maximum temperature deviation D_t, and repeatability half-range F_t were used to evaluate the chamber temperature distribution:

$$R_t = \max_{i,j}(T_{ij}) - \min_{i,j}(T_{ij})$$

$$D_t = \max_{i,j}\left|T_{ij} - T_{\text{set}}\right|$$

$$F_t = \max_i \left[\frac{\max_j(T_{ij}) - \min_j(T_{ij})}{2}\right]$$

where T_{set} is the target temperature. The spatial temperature range describes the overall temperature difference among all monitoring results, the maximum temperature deviation represents the largest absolute difference from the target temperature, and the repeatability half-range characterizes the variation among the three repeated numerical calculations at the same monitoring point. For comparison, R_t and D_t were expressed relative to a reference value of 2.0 °C, whereas F_t was expressed relative to a reference value of 0.5 °C.

III. RESULT

3.1 Temperature fields and airflow pathlines

Figures 3–7 present the static-temperature contours and airflow pathlines obtained at the five target temperatures. Under all operating conditions, airflow formed a continuous recirculation path through the test zone and surrounding gallery. The overall pathline topology remained similar as the inlet temperature changed, indicating that the circulation system maintained a stable airflow pattern over the investigated temperature range.

Across the five cases, the pathlines were concentrated along the upper return passage, passed through the central test region, and turned at both ends of the chamber. The greatest curvature and trajectory intersection occurred in the end-turning and central transition regions, where local temperature gradients were also most visible. The section-based results in Figures 3 and 5–7 showed that the upper plane at Y = 9.5 m was comparatively uniform except for a localized disturbance near the upstream turning region, whereas the middle and lower planes contained elongated temperature bands aligned with the test-platform and wind-tunnel passages. The updated three-dimensional field in Figure 4 further shows the spatial extent of the temperature distribution and the associated circulation path at −10 °C.

At −40 °C, the chamber temperature was generally uniform. A weak warmer region extended along the internal test passage, whereas the surrounding return-air region remained close to the target temperature. The temperature gradients were mainly concentrated near the central passage and airflow-turning regions.

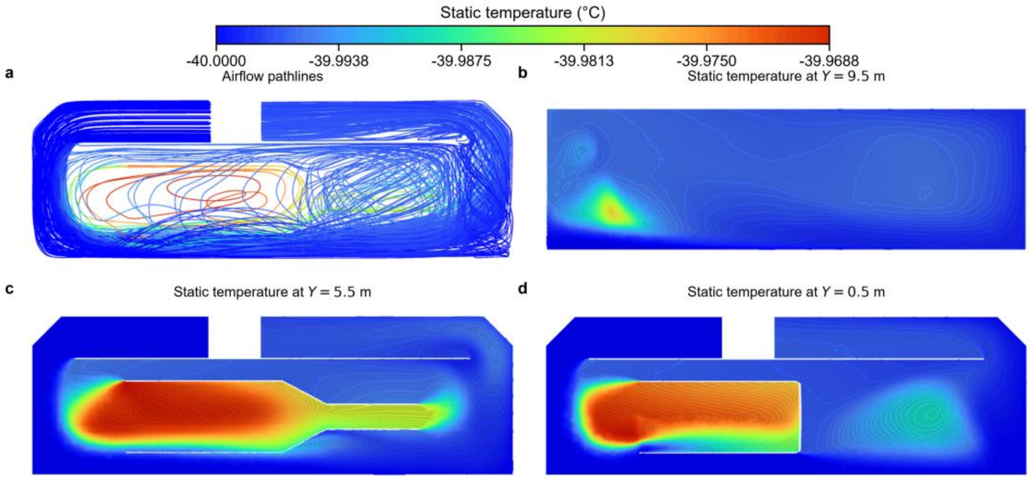

Figure 3: Numerical fields at a target temperature of −40 °C: (a) airflow pathlines coloured by static temperature; static-temperature contours at (b) Y = 9.5 m, (c) Y = 5.5 m, and (d) Y = 0.5 m. The four panels share the horizontal static-temperature colour scale shown above.

The updated −10 °C results showed an elongated warmer region along the internal test and wind-tunnel passages, while the surrounding return-flow region remained closer to the target temperature. The airflow pathlines completed a continuous circulation loop and became more intertwined near the central transition and downstream turning regions. The spatial correspondence between the temperature field and airflow pathlines indicated that the local temperature differences were associated with airflow redistribution along the main circulation path.

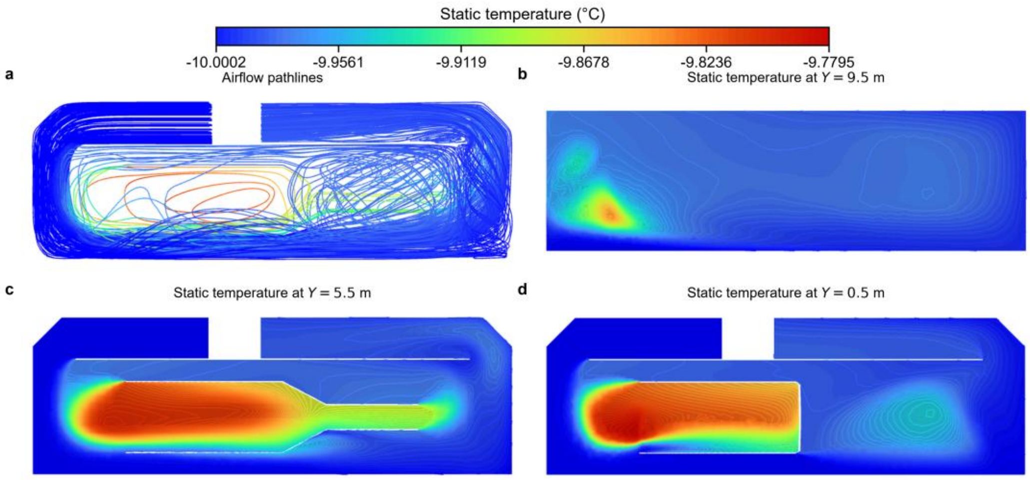

Figure 4: Updated numerical fields at a target temperature of −10 °C: (a) three-dimensional static-temperature contours; (b) airflow pathlines coloured by static temperature. Both panels share the horizontal static-temperature colour scale shown above.

At 0 °C, the temperature field was the most uniform among the five conditions. No distinct large-scale warmer or cooler region was observed. Although slight temperature variations remained near the internal passage and turning regions, the absolute temperature difference was small throughout the chamber.

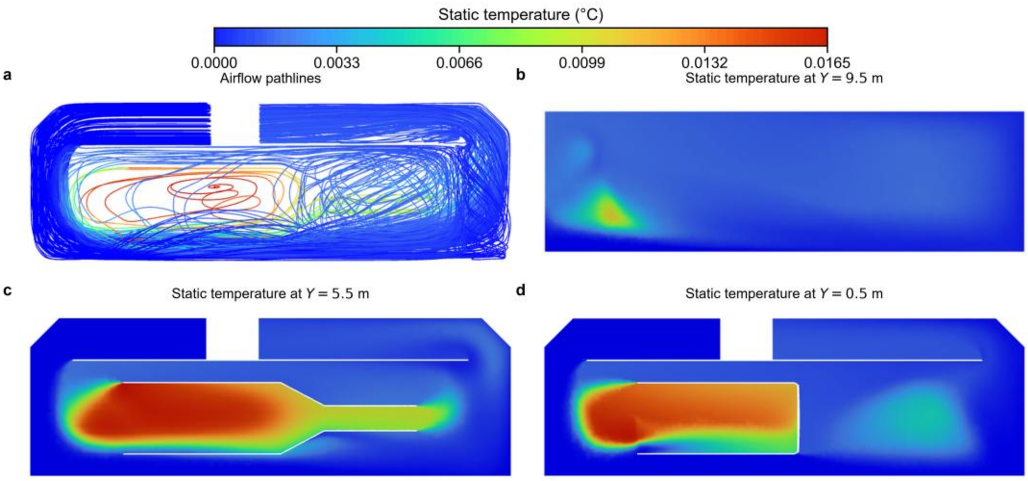

Figure 5: Numerical fields at a target temperature of 0 °C: (a) airflow pathlines coloured by static temperature; static-temperature contours at (b) Y = 9.5 m, (c) Y = 5.5 m, and (d) Y = 0.5 m. The four panels share the horizontal static-temperature colour scale shown above.

Under the 45 °C condition, most of the chamber remained close to the target temperature, but an elongated cooler region appeared within the internal passage. The cooler region was more apparent in the middle and lower sections and extended along the principal airflow direction. This condition exhibited the largest spatial temperature variation among the five investigated cases.

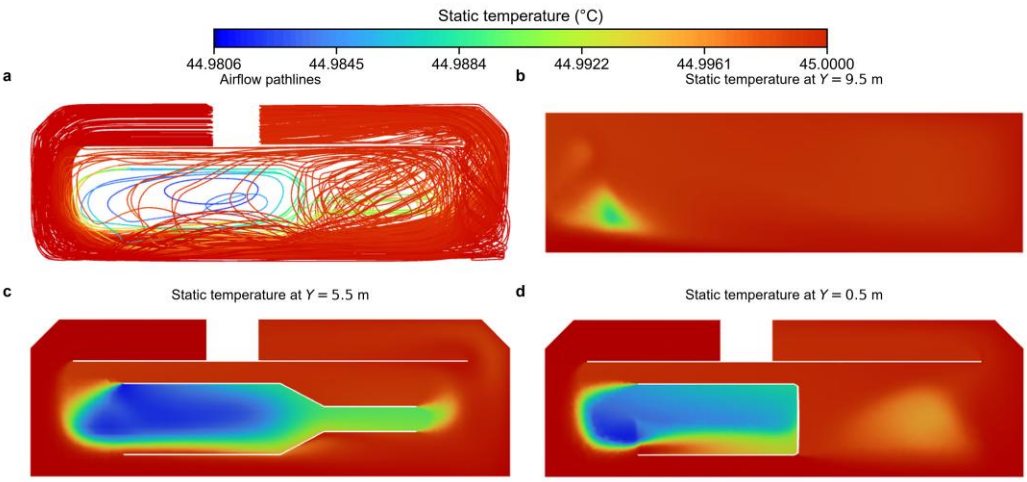

Figure 6: Numerical fields at a target temperature of 45 °C: (a) airflow pathlines coloured by static temperature; static-temperature contours at (b) Y = 9.5 m, (c) Y = 5.5 m, and (d) Y = 0.5 m. The four panels share the horizontal static-temperature colour scale shown above.

At 60 °C, a weak cooler band remained within the internal passage, but its extent and temperature gradient were smaller than those observed at 45 °C. The transition between the internal passage and surrounding return-air region was relatively smooth, and the overall temperature distribution remained uniform.

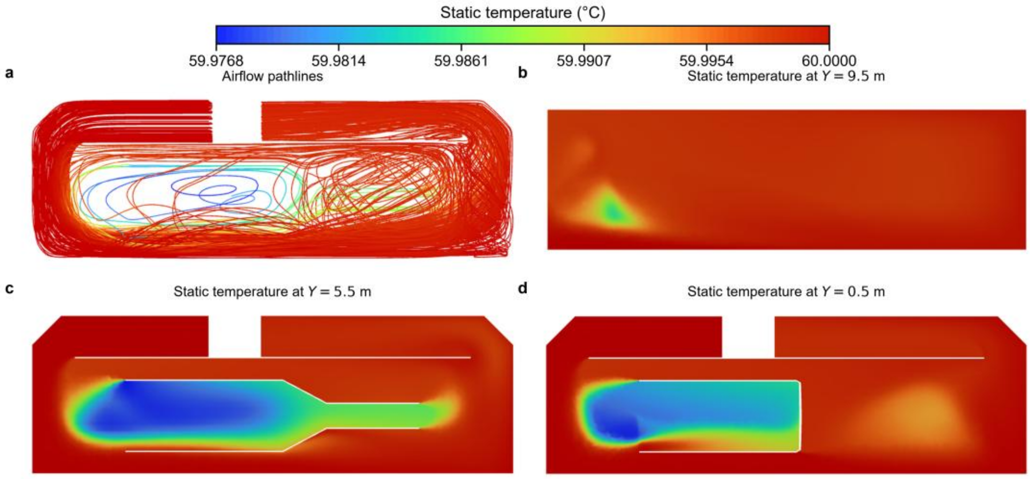

Figure 7: Numerical fields at a target temperature of 60 °C: (a) airflow pathlines coloured by static temperature; static-temperature contours at (b) Y = 9.5 m, (c) Y = 5.5 m, and (d) Y = 0.5 m. The four panels share the horizontal static-temperature colour scale shown above.

3.2 Temperature characteristics at the monitoring points

Figure 8 compares the temperature deviations at the 13 monitoring points. Each plotted value represents the mean of three repeated numerical calculations, while the shaded region represents the corresponding minimum–maximum range. The calculated temperatures at all monitoring points were close to their respective target temperatures.

At −40 °C, the monitoring-point temperatures ranged from −39.999 to −39.969 °C, with an overall mean of −39.983 °C. At −10 °C, the calculated temperatures ranged from −9.996 to −9.901 °C, with an overall mean of −9.950 °C. The largest individual deviation under this condition was 0.099 °C and occurred at monitoring point 10. At 0 °C, the temperature ranged from 0.000 to 0.016 °C, representing the smallest spatial range among the five operating conditions.

Under the heating conditions, the calculated temperatures ranged from 44.894 to 45.000 °C at the 45 °C target and from 59.977 to 60.000 °C at the 60 °C target. At 45 °C, a local minimum of 44.894 °C occurred at monitoring point 9, corresponding to the cooler region shown in the temperature contours. The overall mean temperatures were 44.988 and 59.988 °C at the 45 and 60 °C targets, respectively.

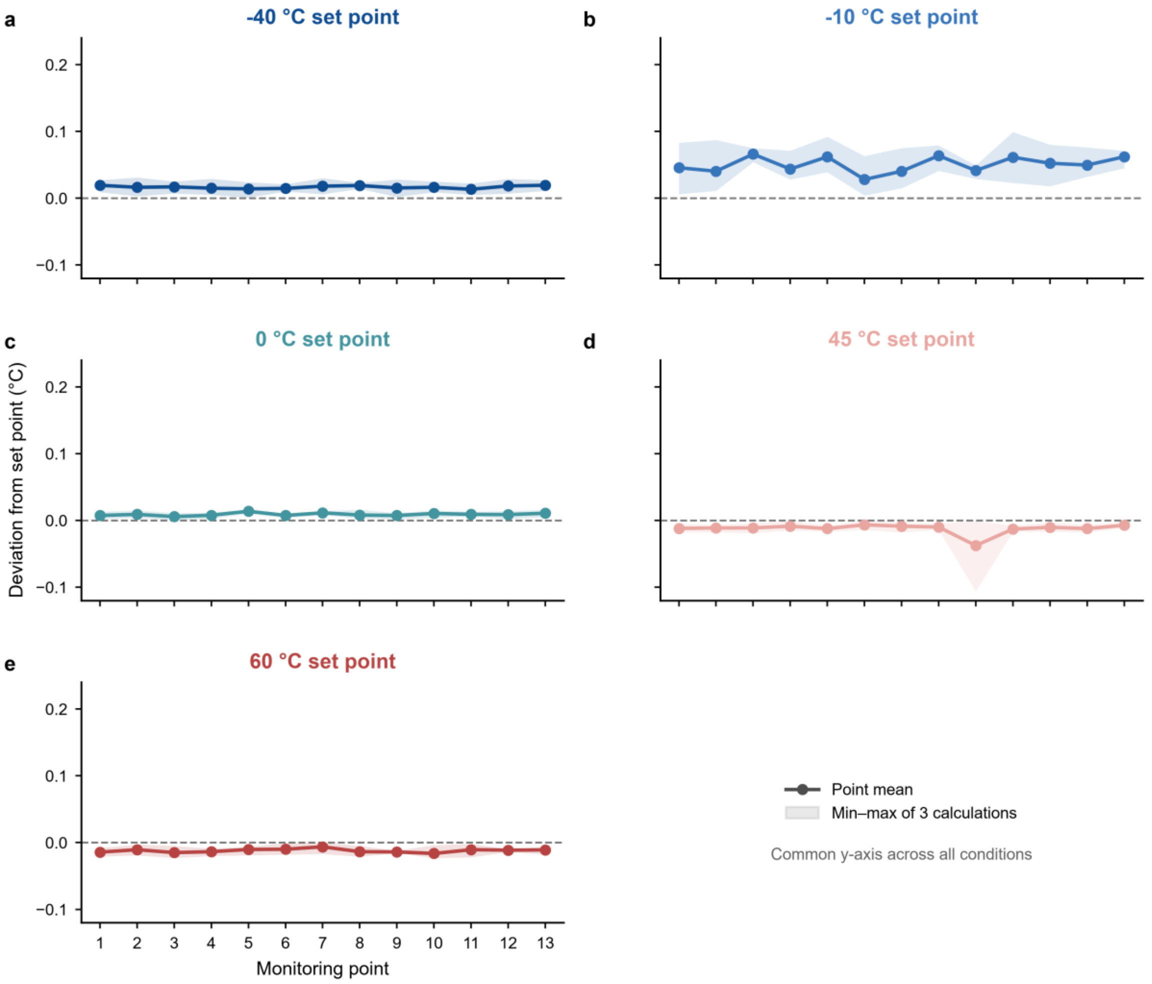

Figure 8: Temperature deviations at the 13 monitoring points under different target-temperature conditions. Symbols represent the means of three repeated numerical calculations, and shaded regions represent the corresponding minimum–maximum ranges.

Table 3. Summary of the numerical temperature-uniformity results.

Target (°C)	Observed range (°C)	Mean (°C)	R_t (°C)	D_t (°C)	F_t (°C)
−40	−39.999 to −39.969	−39.983	0.030	0.031	0.014
−10	−9.996 to −9.901	−9.950	0.095	0.099	0.039
0	0.000 to 0.016	0.009	0.016	0.016	0.007
45	44.894 to 45.000	44.988	0.106	0.106	0.053
60	59.977 to 60.000	59.988	0.023	0.023	0.010

3.3 Temperature-uniformity indicators

Figure 9 compares the spatial temperature range $\boldsymbol{R_t}$, maximum temperature deviation $\boldsymbol{D_t}$, and repeatability half-range $\boldsymbol{F_t}$ under the five operating conditions. The maximum $\boldsymbol{R_t}$ and $\boldsymbol{D_t}$ values both occurred at 45 °C and were 0.106 °C, corresponding to 5.3% of the 2.0 °C reference value. The repeatability half-range at 45 °C was 0.053 °C, corresponding to 10.5% of the 0.5 °C reference value.

The −10 °C condition exhibited the second-largest temperature variation. Its $\boldsymbol{R_t}$, $\boldsymbol{D_t}$, and $\boldsymbol{F_t}$ values were 0.095, 0.099, and 0.039 °C, respectively. The corresponding values at 0 °C were 0.016, 0.016, and 0.007 °C, which were the lowest among the five conditions. The results therefore showed that the temperature field was most uniform at 0 °C and exhibited its largest variation at 45 °C.

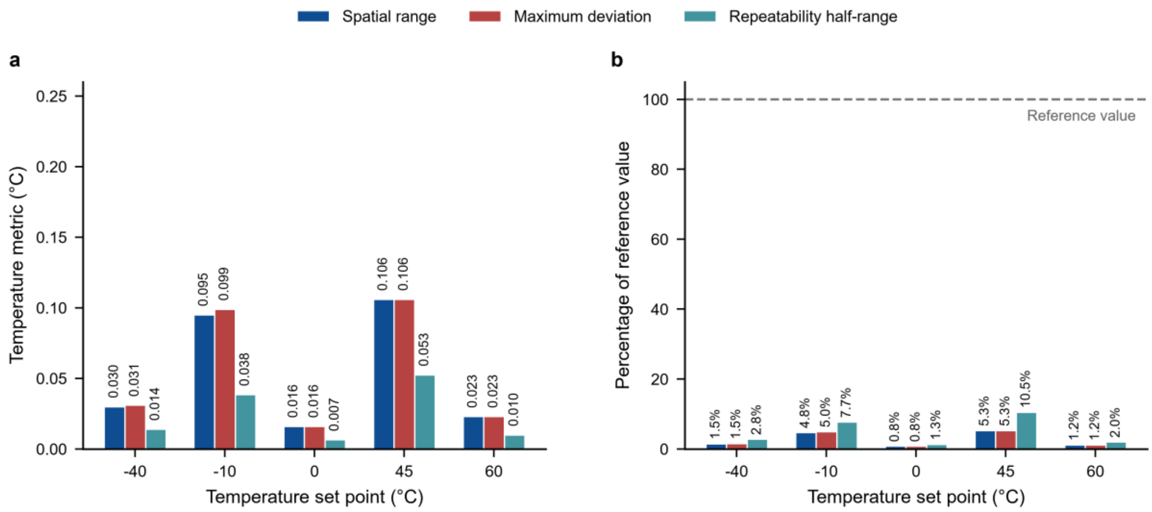

Figure 9: Comparison of the spatial temperature range R_t, maximum temperature deviation D_t, and repeatability half-range F_t under different target-temperature conditions. Panel (b) presents the percentages relative to reference values of 2.0 °C for R_t and D_t and 0.5 °C for F_t.

Figure 10 shows the signed mean temperature deviations at the 13 monitoring points. The cooling conditions generally produced small positive deviations, whereas the heating conditions produced small negative deviations. At −10 °C, the mean deviations ranged from +0.028 to +0.066 °C. At 45 °C, monitoring point 9 showed the largest negative mean deviation of −0.038 °C. The distribution of the signed deviations was consistent with the local warmer and cooler regions observed in the corresponding temperature fields.

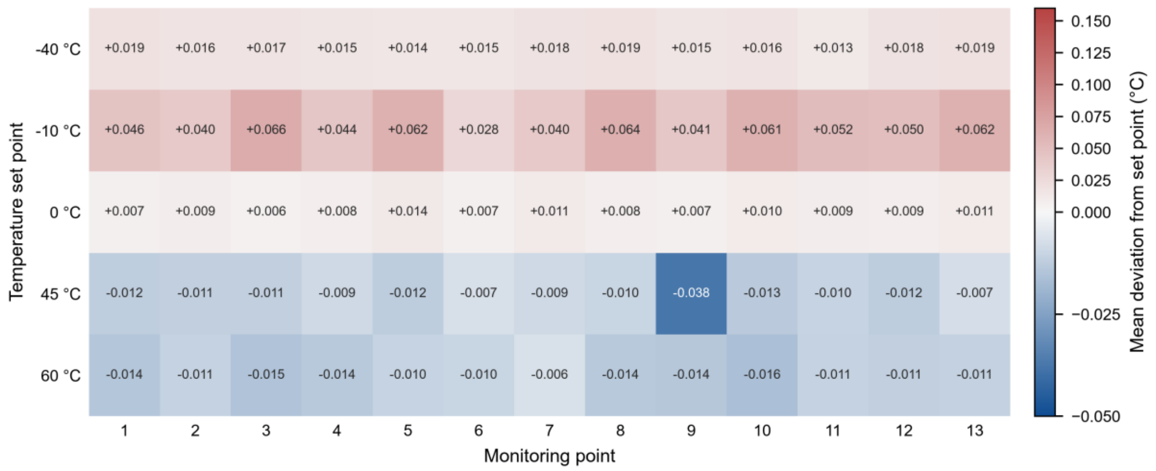

Figure 10: Heatmap of the signed mean temperature deviations at the 13 monitoring points. Positive values indicate temperatures above the target temperature, and negative values indicate temperatures below the target temperature.

IV. DISCUSSION

4.1 Overall temperature-uniformity performance

The numerical results show that the closed-loop circulating air-supply system maintained relatively uniform thermal conditions over the investigated temperature range of -40 to 60°C. The temperature range and maximum deviation from the target temperature did not exceed 0.106°C, and the maximum temperature fluctuation was 0.053°C. Compared with the reference values of 2.0°C for the temperature range and maximum temperature deviation, the largest calculated value accounted for only 5.3% of the reference value. This indicates that the ten axial-flow fans and the surrounding return-air gallery can effectively reduce large-scale temperature gradients within the chamber.

Previous numerical and experimental studies have demonstrated that the thermal performance of climatic chambers is strongly affected by airflow circulation, fan arrangement and inlet configuration. In the present chamber, the ten fans supplied air into a common circulation passage, while the surrounding gallery returned the airflow to the upstream section. This arrangement formed a continuous circulation path and promoted heat exchange between different regions. The overall temperature uniformity therefore resulted from the combined effects of sufficient circulating airflow and the closed-loop airflow organization.

The temperature-uniformity indices did not vary monotonically with the target temperature. The 0°C condition exhibited the smallest temperature range and maximum deviation, whereas the 45°C condition showed the largest values. The updated -10°C condition produced the second-largest temperature range. These results suggest that spatial temperature uniformity depends not only on the magnitude of the imposed target temperature but also on the interaction between thermal regulation and local airflow distribution.

4.2 Relationship between airflow organization and local temperature differences

The temperature contours and pathline distributions show that the airflow organization remained generally stable under all five operating conditions. After entering the chamber through the fan outlets, the airflow passed through the internal wind-tunnel passage and test zone before returning through the surrounding gallery. This continuous circulation promoted thermal mixing and limited the accumulation of large temperature differences.

Nevertheless, local warmer or cooler bands were observed along the internal passage, particularly near the central transition section and the downstream turning regions. In these areas, variations in the flow direction and effective cross-sectional area caused the pathlines to curve, intersect and redistribute. Similar relationships between airflow redistribution and local temperature non-uniformity have been reported for mechanically ventilated enclosures and controlled-environment facilities. The correspondence between the contour distributions and airflow paths indicates that the local temperature differences in the chamber were closely related to the geometry of the circulation passage.

At -10°C, an elongated region with a relatively higher temperature appeared along the internal wind-tunnel passage, whereas the surrounding return-air region remained closer to the target temperature. The largest monitoring-point deviation occurred at point 10. Under the 45°C condition, a relatively cooler region was formed along the internal passage, and point 9 exhibited the largest local deviation. These results are consistent with the relatively large temperature ranges obtained for these two conditions. In contrast, the temperature contours at 0°C were more evenly distributed, which agreed with the smaller monitoring-point differences.

4.3 Engineering implications

The results demonstrate that the current chamber structure and circulating air-supply system can provide stable airflow circulation and a relatively uniform temperature field over a wide target-temperature range. The combination of multiple axial-flow fans, the central wind-tunnel passage and the surrounding return-air gallery enables the airflow to pass repeatedly through the test zone, thereby reducing spatial temperature differences.

Further improvement of the temperature distribution can focus on the central transition section, airflow turning regions and the local areas corresponding to monitoring points 9 and 10. Appropriate adjustment of the airflow allocation among the axial-flow fans, together with optimization of guide structures and passage geometry, may reduce local recirculation and improve air mixing. The established CFD model can therefore be used to compare alternative fan arrangements, airflow rates and internal structural configurations, providing support for subsequent optimization of large climatic chambers.

V. CONCLUSION

Across the investigated temperature range of −40 to 60 °C, the closed-loop air circulation system maintained a relatively uniform thermal environment within the test zone. All three temperature-uniformity indices remained below 0.11 °C. The best uniformity was obtained at 0 °C, while relatively larger spatial variations occurred at 45 °C, indicating that temperature uniformity is closely associated with airflow organization rather than varying monotonically with the target temperature.The remaining temperature differences were mainly concentrated in the central transition section, airflow-turning regions and internal passages. These locations should therefore be prioritized when adjusting fan airflow allocation, introducing flow-guiding structures or improving passage geometry. The results provide a quantitative basis for optimizing the circulation-system design and operating conditions of large climatic environmental chambers.

REFERENCES

[1]. LIANG Y Y, HU J C, CHEN J P, et al. A transient thermal model for full-size vehicle climate chamber[J]. Energy and Buildings, 2014, 85: 256-264. DOI: 10.1016/j.enbuild.2014.09.020.

[2]. SILVA R, BRETT M, FERREIRA A D, et al. Computational Fluid Dynamics Modeling and Experimental Validation of the Thermofluidic Performance of Climatic Chambers[J]. Journal of Thermal Science and Engineering Applications, 2020, 12(2): 021014. DOI: 10.1115/1.4043808.

[3]. RAMEZANI B, TADEU A, JESUS T, et al. Evaluation of the Thermofluidic Performance of Climatic Chambers: Numerical and Experimental Studies[J]. Fluids, 2021, 6(12): 433. DOI: 10.3390/fluids6120433.

[4]. [4] PU L, LI Y Z, ZHU Y H, et al. Experimental and Numerical Investigation on Humidity Distribution in an Environmental Chamber[J]. Journal of Environment and Engineering, 2009, 4(2): 326-337. DOI: 10.1299/jee.4.326.
[5]. PU L, LI Y Z, XIAO F, et al. Effects of different inlet vent positions on the uniformity of humidity inside a building chamber[J]. Energy and Buildings, 2014, 76: 565-571. DOI: 10.1016/j.enbuild.2014.03.022.
[6]. OONO S, MURAKAMI S, MORIKAWA Y, et al. A Development of a Numerical Indoor Climate Chamber: Verification of Basic Performance[J]. Journal of Architecture and Planning (Transactions of AIJ), 2002, 67(553): 85-90. DOI: 10.3130/aija.67.85_3.
[7]. ASTORRI F J, SACAMOTO F S. Use of CFD Simulation to Predict Fan Power and Airflow Pattern Inside the Climatic Chamber[C]. SAE Technical Paper Series, 2004: 2004-01-3254. DOI: 10.4271/2004-01-3254.
[8]. XU X, ZHANG Y L, MEI Z, et al. Numerical Simulation and Experimental Investigation of Flow Fields in Vehicle Climatic Chambers[J]. China Mechanical Engineering, 2023, 34(17): 2115-2123. DOI: 10.3969/j.issn.1004-132X.2023.17.011.
[9]. ANGELOVA R A, MIJORSKI S, MARKOV D, et al. Numerical Modelling of the Draught Rate in a Mechanically Ventilated Climate Chamber[J]. Journal of Physics: Conference Series, 2021, 1730(1): 012095. DOI: 10.1088/1742-6596/1730/1/012095.
[10]. OTHMAN F B, DELATTAIGNANT S, ALEXANDRE A L, et al. Development and evaluation of a climatic chamber with the potential to enhance plant resilience and optimize agricultural productivity[J]. Thermal Science and Engineering Progress, 2025, 62: 103645. DOI: 10.1016/j.tsep.2025.103645.
[11]. KOSUTOVA K, VAN HOOFF T, BLOCKEN B. CFD simulation of non-isothermal mixing ventilation in a generic enclosure: Impact of computational and physical parameters[J]. International Journal of Thermal Sciences, 2018, 129: 343-357. DOI: 10.1016/j.ijthermalsci.2018.03.001.
[12]. VAN HOOFF T, BLOCKEN B. Mixing ventilation driven by two oppositely located supply jets with a time-periodic supply velocity: A numerical analysis using computational fluid dynamics[J]. Indoor and Built Environment, 2020, 29(4): 603-620. DOI: 10.1177/1420326X19884667.
[13]. PICHUROV G, STANKOV P. Integration of thermophysiological body model in CFD[J]. Open Engineering, 2013, 3(3): 513-521. DOI: 10.2478/s13531-012-0071-8.
[14]. ZHANG Y, KACIRA M, AN L. A CFD study on improving air flow uniformity in indoor plant factory system[J]. Biosystems Engineering, 2016, 147: 193-205. DOI: 10.1016/j.biosystemseng.2016.04.012.
[15]. ZHANG Y, KACIRA M. Analysis of climate uniformity in indoor plant factory system with computational fluid dynamics (CFD)[J]. Biosystems Engineering, 2022, 220: 73-86. DOI: 10.1016/j.biosystemseng.2022.05.009.
[16]. LAUNDER B E, SPALDING D B. The numerical computation of turbulent flows[J]. Computer Methods in Applied Mechanics and Engineering, 1974, 3(2): 269-289. DOI: 10.1016/0045-7825(74)90029-2.